2D Materials

CrossMark

PAPER

Resolving spin currents and spin densities generated by charge-spin interconversion in systems with reduced crystal symmetry

Lorenzo Camosi[1,*], Josef Světlík[1,2] (iD), Marius V Costache[1] (iD), Williams Savero Torres[1],
Iván Fernández Aguirre[1,2], Vera Marinova[3] (iD), Dimitre Dimitrov[3,4] (iD), Marin Gospodinov[4], Juan F Sierra[1] (iD)
and Sergio O Valenzuela[1,5,*] (iD)

[1] Catalan Institute of Nanoscience and Nanotechnology (ICN2), CSIC and The Barcelona Institute of Science and Technology (BIST),
  Campus UAB, Bellaterra, 08193 Barcelona, Spain
[2] Universitat Autònoma de Barcelona, Bellaterra, 08193 Barcelona, Spain
[3] Institute of Optical Materials and Technologies, Bulgarian Academy of Science, 1113 Sofia, Bulgaria
[4] Institute of Solid State Physics, Bulgarian Academy of Sciences, 1784 Sofia, Bulgaria
[5] Institució Catalana de Recerca i Estudis Avançats (ICREA), 08010 Barcelona, Spain
[*] Authors to whom any correspondence should be addressed.

E-mail: lorenzo.camosi@gmail.com **and** SOV@icrea.cat

Abstract

The ability to control the generation of spins in arbitrary directions is a long-sought goal in spintronics. Charge to spin interconversion (CSI) phenomena depend strongly on symmetry. Systems with reduced crystal symmetry allow anisotropic CSI with unconventional components, where charge and spin currents and the spin polarization are not mutually perpendicular to each other. Here, we demonstrate experimentally that the CSI in graphene-WTe$_2$ induces spins with components in all three spatial directions. By performing multi-terminal nonlocal spin precession experiments, with specific magnetic fields orientations, we discuss how to disentangle the CSI from the spin Hall and inverse spin galvanic effects.

1. Introduction

In condensed matter, spin orbit coupling (SOC) and (broken) crystal and temporal symmetries play a fundamental role, strongly modifying the electronic states and connecting spin and orbital angular momentum degrees of freedom [1]. Their action leads to novel physical states, such as topological phases [2–5], and technologically relevant electron-spin transport phenomena, such as charge-spin interconversion (CSI) [6–9]. The spin Hall effect (SHE) [7, 10–12] and inverse spin galvanic effect (ISGE) [13] (and the corresponding reciprocal effects according to the Onsager relationships [14, 15]) are fundamental CSI phenomena that have been broadly investigated as spin generators and detectors [6–8]. In the conventional SHE, an electrical current induces a transverse spin current. The basic mechanism can have extrinsic or intrinsic origin [7]; the former involves Mott scattering with impurities, while the

latter is closely connected to the Berry curvature [5, 16, 17]. In the ISGE, also known as Rashba-Edelstein effect [18], an electrical current induces a non-equilibrium spin density. The ISGE results from a redistribution of charge carriers on the Fermi surface in systems having a momentum-asymmetric spin texture, which derives from broken inversion symmetry, either structural (e.g. surface or interface) or in the bulk (*i.e.* crystal lattice) [19, 20].

Experimental observations of the SHE and ISGE were originally obtained in semiconductors [13, 21, 22] and metals [23–25]. Even though it was known that, given their SOC-related origin, the SHE and ISGE are often concomitant, those early works usually focused on either the SHE or the ISGE (and their reciprocals). However, understanding the relation between the SHE and ISGE has become essential in light of their potential technological relevance, in particular for electrically reorienting magnets for memory applications [7, 26]. Research on SHE and

ISGE has been further stimulated by recent results in van der Waals heterostructures [27] and, more specifically, in graphene in proximity with high-SOC materials, in which the CSI efficiency is found to be relatively large [28–30].

In some cases, it is possible to discriminate between the SHE and ISGE as, for instance, when graphene is modified by the proximity of a semiconducting transition metal dichalcogenide (TMDC) in high-symmetry heterostructures. There, the SHE and ISGE are driven by valley-Zeeman and conventional Rashba SOC, respectively, leading to spin populations that are orthogonal to each other [31, 32] and, therefore, that can be easily disentangled [28, 30, 33]. This is not the case when the TMDC is conducting, as separating contributions deriving from currents in the TMDC bulk and in the interface or in proximitized graphene is not straightforward [27, 29]. In addition, if the TMDC is a low-symmetry material, such as $MoTe_2$ or WTe_2, or twisting between graphene and the TMDC results in a heterostructure with reduced-symmetry, CSI with unconventional spin orientations can be expected [34–37].

Spin-torque experiments have proposed the presence of unconventional torques compatible with the WTe_2 symmetries [38]. However, recent studies in graphene-$MoTe_2$ and graphene-WTe_2 nonlocal spin devices, not only have not observed the new CSI contribution but found instead a component of unknown origin [34, 36], which was ascribed to broken symmetries due to uncontrolled strain during device fabrication. These measurements were carried out without characterization of the strain or direct knowledge of the crystal orientation, although it has been argued that the crystals typically cleave in a favored direction [34]. Furthermore, a recent study suggests that a widespread method to identify the ISGE (SGE) by rotating the magnetization of the ferromagnetic (FM) detector (injector) is unreliable [39]. These observations demonstrate that it is necessary to carry out additional experiments and to establish nonlocal measurement schemes to identify and quantify competing CSI effects in combination with crystal-orientation and strain characterization in the same device.

In this work, we present a measurement protocol based on spin precession for resolving the contributions of SHE and ISGE [30, 39, 40]. We then implement a graphene-WTe_2 device and demonstrate the generation of spins oriented within and perpendicular to the graphene plane. Although an out-of-plane spin polarization by CSI is expected due to the crystal symmetry in thin WTe_2 layers, it has never been observed in hybrid graphene-WTe_2 heterostructures. Here, we detect it for the first time, demonstrating that this system enables spin generation with all three spatial orientations. The WTe_2 crystal orientation is determined by means of polarized Raman spectroscopy, which also characterizes the crystal strain.

Based on these observations, the possible origins of the observed CSI components are discussed.
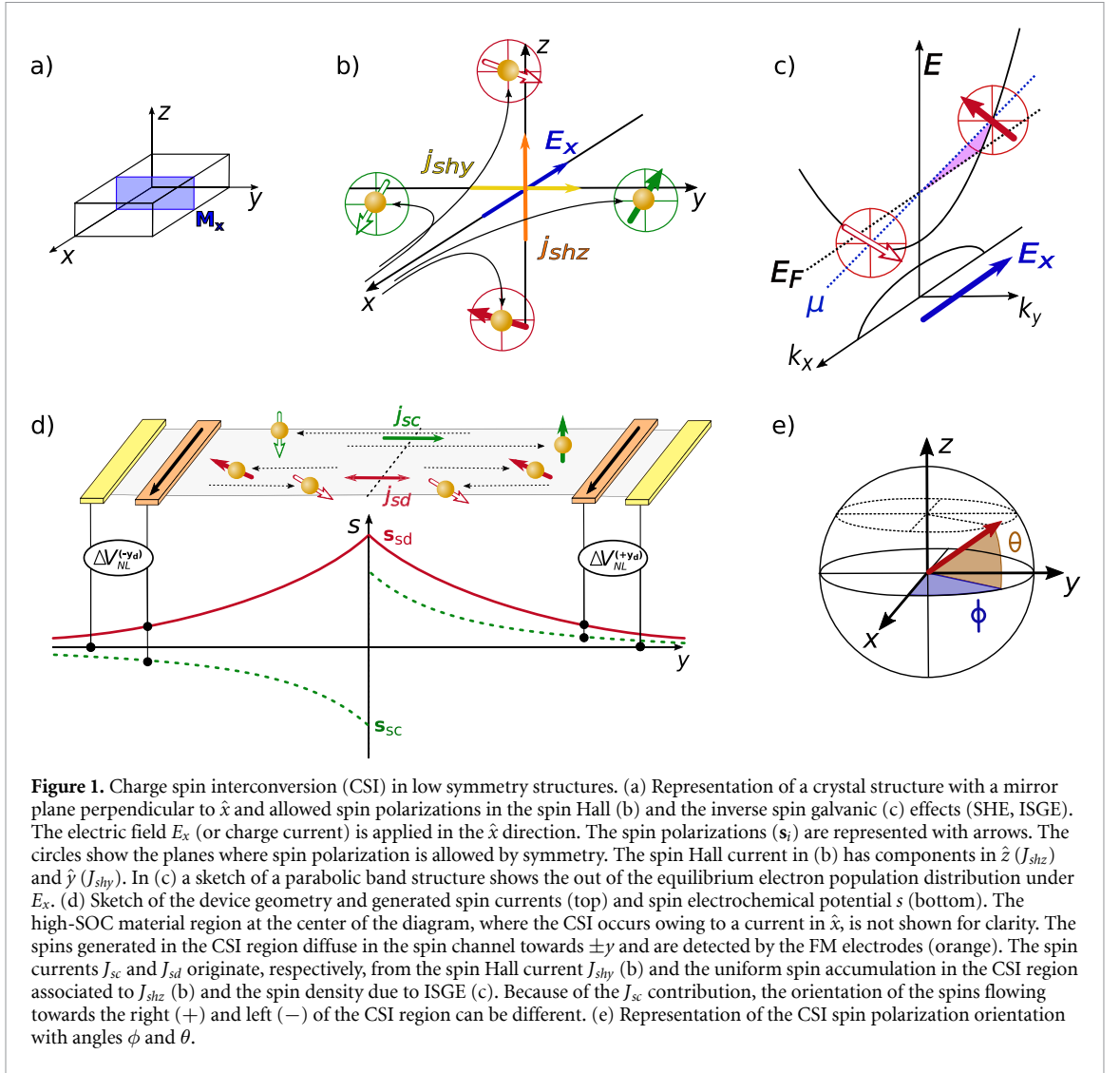
2. Results and discussion

2.1. CSI and crystal symmetries
The character of the CSI is dictated by crystal symmetries. The SHE is described by linear response theory [41] as $j_i^k = \sigma_{ij}^k E_j$, where E_j is the external electric field in the $\hat{j}$ direction that generates a charge current $\mathbf{j}_c$, j_i^k the spin current in the $\hat{i}$ direction with spin polarization $\mathbf{s}$ in the $\hat{k}$ direction and σ_{ij}^k the spin conductivity tensor. In a high-symmetry crystal only off-diagonal σ_{ij}^k terms with $i \neq j \neq k$ are non-zero, resulting in ($\mathbf{j}_c \perp \mathbf{j}_s \perp \mathbf{s}$). Reduced symmetries allow additional σ_{ij}^k elements that can break the mutual perpendicular relationship between $\mathbf{j}_c, \mathbf{j}_s$ and $\mathbf{s}$ [41, 42]. For example, in a crystal with a single mirror plane, as depicted in figure 1(a), a $\mathbf{j}_c$ perpendicular to the plane can lead to $\mathbf{s}$ parallel to the transverse $\mathbf{j}_s$ (figure 1(b)) but mirror symmetry still precludes a transverse $\mathbf{j}_s$ with an $\mathbf{s}$ component along $\mathbf{j}_c$. The latter restriction disappears if the mirror symmetry is broken. The ISGE depends directly on the electronic band structure polarization but it is governed by the same symmetry considerations [19, 20]. In a high symmetry crystal, non-zero spin density could only arise at a boundary or interface, leading to the conventional Rashba effect [43, 44]. In figure 1(a), the mirror symmetry imposes that the spin polarization must be contained in the mirror plane (figure 1(c)).

2.2. Resolving SHE and ISGE in nonlocal devices
Nonlocal spin-dependent measurements have been widely used to investigate CSI phenomena [7, 23] and extract the polarization of the generated spins. There, a charge current I is applied along the CSI region and the nonlocal voltage ΔV_{NL} is measured between a FM detector and a reference outer metallic contact as a function of the orientation and magnitude of an applied magnetic field $\mathbf{B}$ [23, 40, 45]. When the spins originating from the SHE and the ISGE are perpendicular to each other, they can be fully resolved by investigating spin precession with in-plane and perpendicular magnetic fields [30] or by means of a symmetry analysis under oblique magnetic fields [28, 33]. These approaches are not sufficient in graphene-WTe_2 or graphene-$MoTe_2$ heterostructures, where the TMDC is conducting and has low-symmetry [34, 36, 46]. However, in such systems the ISGE induces a local spin density, whereas the SHE induces a directed spin current. Therefore, it is possible to discern between the SHE and ISGE generated spins by simultaneously measuring the spin accumulation along the spin-current direction at opposite sides of the CSI region, as illustrated in figure 1(d).

When the current I is applied along $\hat{x}$ in the CSI region (not shown in the figure 1(d)), the
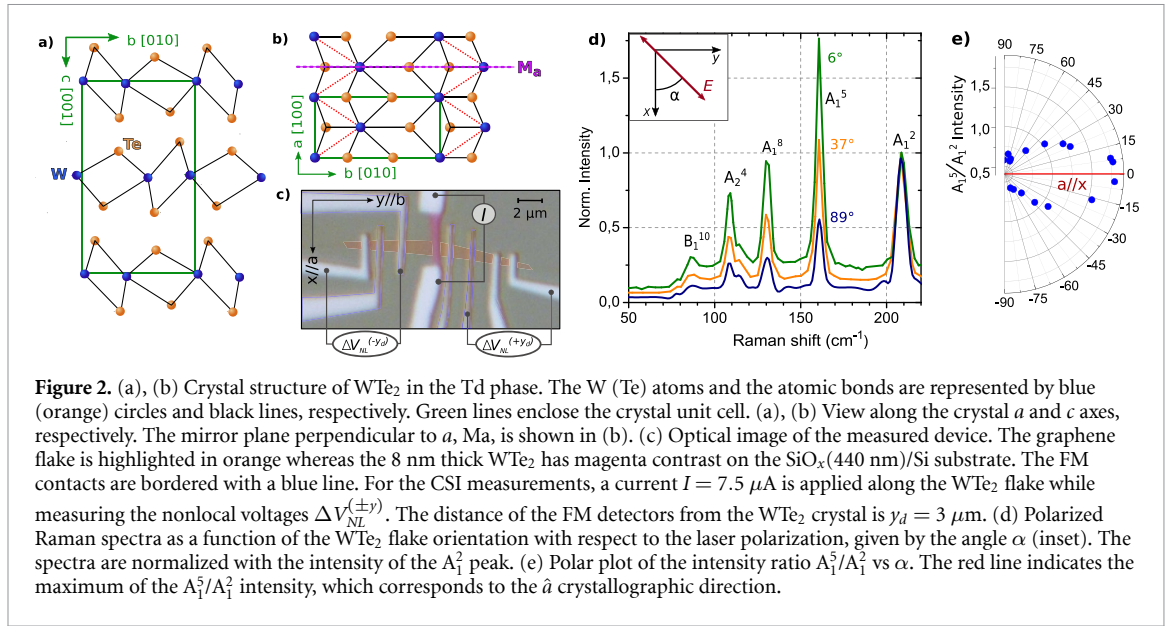
Figure 1. Charge spin interconversion (CSI) in low symmetry structures. (a) Representation of a crystal structure with a mirror plane perpendicular to $\hat{x}$ and allowed spin polarizations in the spin Hall (b) and the inverse spin galvanic (c) effects (SHE, ISGE). The electric field E_x (or charge current) is applied in the $\hat{x}$ direction. The spin polarizations (s_i) are represented with arrows. The circles show the planes where spin polarization is allowed by symmetry. The spin Hall current in (b) has components in $\hat{z}$ (J_{shz}) and $\hat{y}$ (J_{shy}). In (c) a sketch of a parabolic band structure shows the out of the equilibrium electron population distribution under E_x. (d) Sketch of the device geometry and generated spin currents (top) and spin electrochemical potential s (bottom). The high-SOC material region at the center of the diagram, where the CSI occurs owing to a current in $\hat{x}$, is not shown for clarity. The spins generated in the CSI region diffuse in the spin channel towards $\pm y$ and are detected by the FM electrodes (orange). The spin currents J_{sc} and J_{sd} originate, respectively, from the spin Hall current J_{shy} (b) and the uniform spin accumulation in the CSI region associated to J_{shz} (b) and the spin density due to ISGE (c). Because of the J_{sc} contribution, the orientation of the spins flowing towards the right (+) and left (−) of the CSI region can be different. (e) Representation of the CSI spin polarization orientation with angles ϕ and θ.

SHE creates spin currents along $\hat{y}$ (J_{shy}) and $\hat{z}$ (J_{shz}) (figure 1(b)), which coexist with the spin density induced by the ISGE (figure 1(c)). A direct comparison between ΔV_{NL} at $\pm y$, $\Delta V_{NL}^{(\pm y)}$, differentiates the spins associated to the spin current J_{shy} from those associated to the ISGE and J_{shz} (figure 1(d)). Indeed, the spin current component J_{sc} diffusing away from the CSI region, which originates from J_{shy}, generates opposite spin accumulation at $\pm y$, while the spin current J_{sd}, associated to the ISGE and J_{shz}, generates equal spin accumulation at $\pm y$. Therefore, $(\Delta V_{NL}^{(+y)} + \Delta V_{NL}^{(-y)})/2 \propto J_{sd}$ whereas $(\Delta V_{NL}^{(+y)} - \Delta V_{NL}^{(-y)})/2 \propto J_{sc}$. Such measurements do not distinguish between the ISGE and J_{shz}, since both induce a spin accumulation whose orientation does not vary in the CSI region [29]. Nevertheless, these components can in principle be disentangled by analyzing $(\Delta V_{NL}^{(+y)} + \Delta V_{NL}^{(-y)})/2$ as a function of the SOC-material thickness [7]. In particular, when the thickness is much smaller than the spin relaxation length along $\hat{z}$, J_{shz} vanishes [47, 48], and only ISGE contributes to the nonlocal signal.

With the previous considerations, we focus on fully characterizing the spins generated by J_{sc} and J_{sd} by means of spin precession using spin detectors located at $\pm y_d$. The steady-state spin diffusion and precession in the spin channel are governed by the Bloch diffusion equation [49–51]:

$$\mathbf{D}\frac{\partial^2 \mathbf{s}}{\partial y^2} + \gamma_c \mathbf{s} \times \mathbf{B} - \mathbf{s} \cdot \overline{\overline{\Gamma}}^{-1} = 0, \qquad (1)$$

where $\mathbf{s} = (s_x, s_y, s_z)$ and s_i is the spin electrochemical potential for spins along i, γ_c is electron gyromagnetic ratio, $\mathbf{D} = (D_x, D_y, D_z)$ is the diffusion constant, and $\overline{\overline{\Gamma}}$ characterizes the spin lifetime τ_i. In the most general case, the injected spins have an arbitrary spin orientation. The CSI spin injection efficiency into the spin channel can be quantified using effective spin-polarization factors $\mathbf{P} = (P_x, P_y, P_z) = (j_x/I, j_y/I, j_z/I)w$, with j_i the corresponding spin currents with contributions from J_{sc} and J_{sd}, and w the width of the channel. Assuming isotropic spin transport in the channel and that the FM detector is characterized by a magnetization along the $+\hat{x}$

Figure 2. (a), (b) Crystal structure of WTe$_2$ in the Td phase. The W (Te) atoms and the atomic bonds are represented by blue (orange) circles and black lines, respectively. Green lines enclose the crystal unit cell. (a), (b) View along the crystal *a* and *c* axes, respectively. The mirror plane perpendicular to *a*, M$_a$, is shown in (b). (c) Optical image of the measured device. The graphene flake is highlighted in orange whereas the 8 nm thick WTe$_2$ has magenta contrast on the SiO$_x$(440 nm)/Si substrate. The FM contacts are bordered with a blue line. For the CSI measurements, a current $I = 7.5\ \mu$A is applied along the WTe$_2$ flake while measuring the nonlocal voltages $\Delta V_{NL}^{(\pm y)}$. The distance of the FM detectors from the WTe$_2$ crystal is $y_d = 3\ \mu$m. (d) Polarized Raman spectra as a function of the WTe$_2$ flake orientation with respect to the laser polarization, given by the angle α (inset). The spectra are normalized with the intensity of the A$_1^2$ peak. (e) Polar plot of the intensity ratio A$_1^5$/A$_1^2$ vs α. The red line indicates the maximum of the A$_1^5$/A$_1^2$ intensity, which corresponds to the $\hat{a}$ crystallographic direction.

direction and by a polarization efficiency P_{FM}, the nonlocal resistance $R_{NL} \equiv \Delta V_{NL}/I$ for **B** along $\hat{y}$ and $\hat{z}$ takes the respective general forms:

$$R_{NL}(B_y) = \frac{R_\square P_{FM}}{4\ w}Re\left[\frac{ie^{-\sqrt{\frac{1-i\tau\omega}{D\tau}}y_d}(P_x + iP_z)}{\sqrt{\frac{1-i\tau\omega}{D\tau}}} + h.c.\right]$$

(2)

$$R_{NL}(B_z) = \frac{R_\square P_{FM}}{4\ w}Re\left[\frac{ie^{-\sqrt{\frac{1-i\tau\omega}{D\tau}}y_d}(P_x - iP_y)}{\sqrt{\frac{1-i\tau\omega}{D\tau}}} + h.c.\right],$$

(3)

where $\omega = \gamma_c B$ and $R_\square$ is the channel sheet resistance.

Fitting the spin precession response to equations (2) and (3) determines **P**. The spin-injection angles for spins moving towards $\pm\hat{y}$, defined as $\theta^\pm \equiv \arctan(P_z^\pm/\sqrt{(P_x^\pm)^2 + (P_y^\pm)^2})$ and $\phi^\pm \equiv \arctan(P_y^\pm/P_x^\pm)$, fully characterize the orientation of the injected spins on both sides of the CSI region (figure 1(e)). Therefore, comparing θ^+ with θ^- and ϕ^+ with ϕ^- provides direct information on J_{sc} and J_{sd}. In addition, focusing on $\theta^\pm$ and $\phi^\pm$, rather than **P**$^\pm$, eliminates errors deriving from potential differences in the FM detector polarizations.
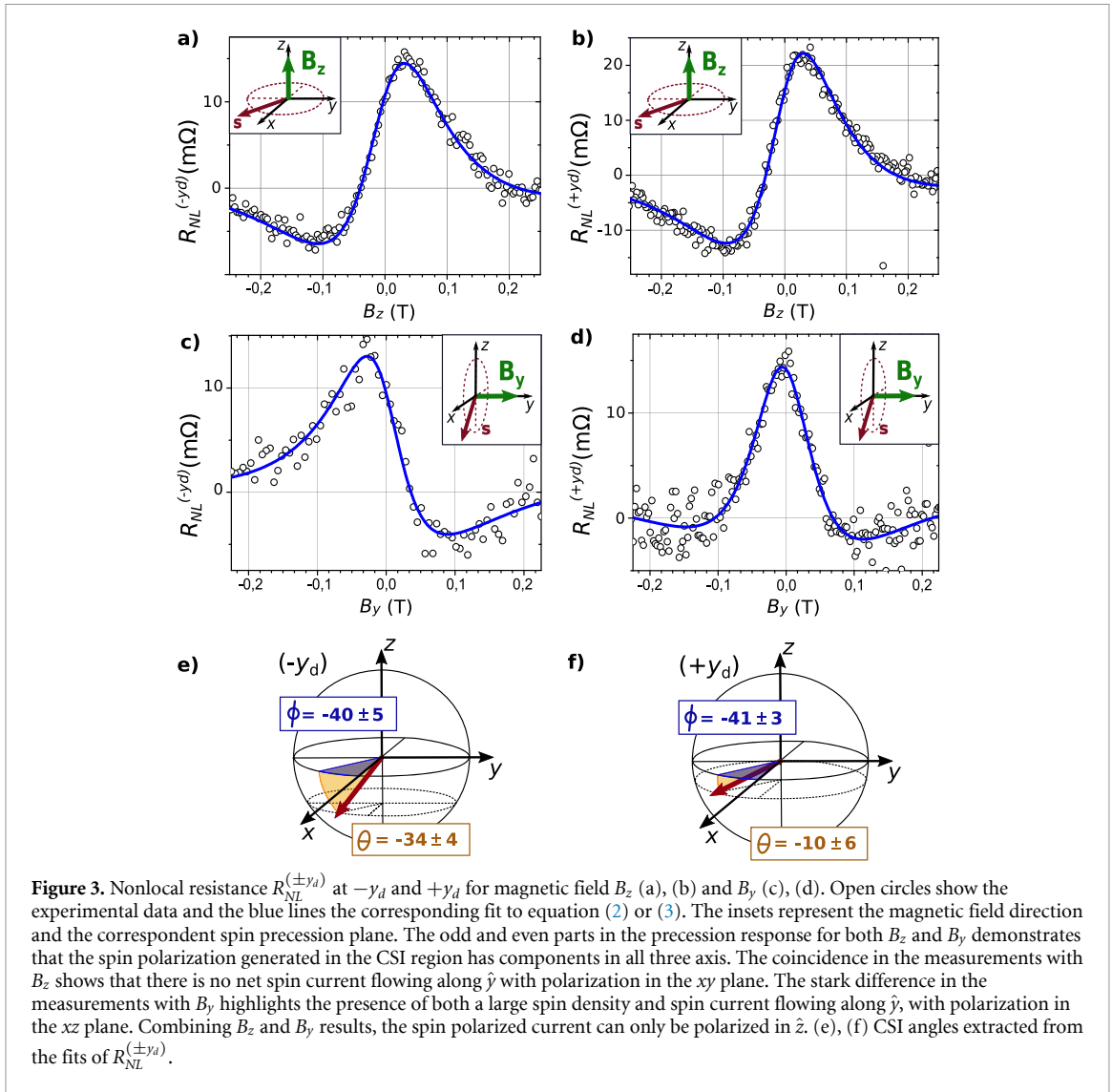
2.3. CSI in graphene-WTe$_2$

WTe$_2$ is a layered TMDC, which is stable in the orthorhombic Td(Pmn2$_1$) phase. It is characterized by a lack of bulk inversion symmetry (figures 2(a) and (b)), a glide mirror plane M_b, an out-of-plane two-fold screw rotational symmetry C_{2c} and a mirror plane M_a perpendicular to the $\hat{a}$ crystallographic direction (figure 2(b)). Multilayer Td-WTe$_2$ is a type-II Weyl semimetal [52, 53] while in monolayer form it is a 2D topological insulator [54–56]. Considering the mirror crystal symmetries, in the SHE, $\mathbf{j}_c \perp \mathbf{j}_s \perp \mathbf{s}$

while, in the ISGE, $\mathbf{j}_c$ along $\hat{a}$ can induce a spin density with spins oriented along $\hat{b}$ and vice versa, but no spin density parallel to $\hat{c}$.

The graphene-WTe$_2$ device fabrication follows the protocols established with other TMDCs [30] (see supplementary information (available online at stacks.iop.org/TDM/9/035014/mmedia)). The WTe$_2$ crystals were grown by chemical vapor transport, using bromine as a transport agent [57]. Their electronic and crystalline structure was investigated by x-ray photoelectron spectroscopy, angle-resolved photoemission spectroscopy, and Raman spectroscopy, all of them demonstrating high quality and confirming the Td phase (see supplementary material). The crystallographic orientation of the WTe$_2$ crystal in the actual device (figure 2(c)) is obtained by means of linearly polarized Raman spectroscopy. Figure 3(d) shows the Raman spectra when the laser polarization is rotated at angle α relative to the long-axis of the WTe$_2$ flake (figure 2(c)). The intensity of the Raman modes A$_1^5$ (164 cm^{-1}) and A$_1^2$ (212 cm^{-1}) are known to change as a function of crystal orientation. As the ratio A$_1^5$/A$_1^2$ is maximum at $\alpha = 0$ (figure 2(e)) then, in our device, $\hat{a} \parallel \hat{x}$ [58].

As the spin transport in graphene on SiO$_2$ is isotropic [59], the parameters τ and D (as well as P_{FM}) in equations (2) and (3) are extracted by measuring spin precession with out-of-plane **B** in the two reference graphene devices at both sides of WTe$_2$. The CSI is then investigated by applying a charge current I along the WTe$_2$ crystal ($\hat{a} \parallel \hat{x}$ direction). All measurements are carried out at room temperature.

Figure 3 shows the nonlocal resistances $R_{NL}^{(+y_d)}$ and $R_{NL}^{(-y_d)}$ as a function of B_y and B_z. The signals have been acquired with the FM magnetizations saturated along both the $\pm\hat{x}$ directions to remove contributions that are unrelated to spin and associated to the magnetization rotation of the FM detector (see

Figure 3. Nonlocal resistance $R_{NL}^{(\pm y_d)}$ at $-y_d$ and $+y_d$ for magnetic field B_z (a), (b) and B_y (c), (d). Open circles show the experimental data and the blue lines the corresponding fit to equation (2) or (3). The insets represent the magnetic field direction and the correspondent spin precession plane. The odd and even parts in the precession response for both B_z and B_y demonstrates that the spin polarization generated in the CSI region has components in all three axis. The coincidence in the measurements with B_z shows that there is no net spin current flowing along $\hat{y}$ with polarization in the xy plane. The stark difference in the measurements with B_y highlights the presence of both a large spin density and spin current flowing along $\hat{y}$, with polarization in the xz plane. Combining B_z and B_y results, the spin polarized current can only be polarized in $\hat{z}$. (e), (f) CSI angles extracted from the fits of $R_{NL}^{(\pm y_d)}$.

supplementary material). Remarkably, $R_{NL}^{(+y_d)}$ and $R_{NL}^{(-y_d)}$ present nearly undistinguishable lineshapes for B_z (figures 3(a) and (b)), while this is clearly not the case for B_y (figures 3(c) and (d)).

For B_z, only the in-plane (xy) components of the injected spins contribute to the precession lineshape. Therefore, the fact that $R_{NL}^{(+y_d)} \sim R_{NL}^{(-y_d)}$ demonstrates that the spins diffusing towards $-\hat{y}$ and $+\hat{y}$ have the same in-plane spin polarization, which is an indication of a uniform in-plane polarization in the CSI region (associated to J_{sd} in figure 1(d)). Moreover, because $R_{NL}^{(\pm y_d)}$ are neither fully symmetric nor fully antisymmetric about $B_z = 0$, the spin polarization has nonzero components along both $\hat{x}$ and $\hat{y}$.

In contrast, for B_y only the spin components in the xz plane contribute to the precession lineshape. The marked difference between $R_{NL}^{(+y_d)}$ and $R_{NL}^{(-y_d)}$ demonstrates that the spins diffusing towards $-\hat{y}$ and $+\hat{y}$ have different spin polarization orientation in the xz plane. Combined with the results for B_z, this observation is an unambiguous indication of a spin polarized current in the CSI region with a

polarization along $\hat{z}$ (associated to J_{sc} in figure 1(d)). Furthermore, $R_{NL}^{(+y_d)}$ being rather symmetric about $B_y = 0$ (figure 3(d)) also demonstrates the presence of a uniform spin density along $\hat{z}$, originating from J_{sd}, which partially compensates the contribution from J_{sc}.

To quantify the relative magnitudes of each CSI component, we fit the measurements in figure 3 to equation (2) or (3). The fittings are shown with blue lines, from which the spin-polarization angles $\theta^\pm$ and $\phi^\pm$ are extracted: $(\phi^-, \theta^-) = (-40° \pm 5°, -34° \pm 4°)$ and $(\phi^+, \theta^+) = (-41° \pm 3°, -10° \pm 6°)$ (see figures 3(e) and (f) for a schematic representation). The spins originating from J_{sd} and J_{sc} relate to $(\phi_s, \theta_s) = [(\phi^+ + \phi^-)/2, (\theta^+ + \theta^-)/2] = (-41° \pm 4°, -22° \pm 5°)$ and $(\phi_{as}, \theta_{as}) = [(\phi^+ - \phi^-)/2, (\theta^+ - \theta^-)/2] = (0 \pm 4°, -12° \pm 5°)$, respectively. The presence of non-zero symmetric and antisymmetric angular components confirms the coexistence in the CSI region of spin-Hall currents along $\hat{y}$ with polarization in $\hat{z}$ and uniform spin densities with polarizations components on $\hat{x}, \hat{y}$ and $\hat{z}$.

2.4. Origin of the observed CSI in graphene-WTe$_2$
Although our experiments establish the presence of CSI with different symmetries, unequivocally identifying the underlying CSI mechanisms requires further analysis. The CSI can originate from either the ISGE or the SHE, in the bulk of WTe$_2$, at the graphene-WTe$_2$ interface or in graphene by proximity effects [27].

The spin density in the CSI region has components in all three directions (figure 3). According to the Td-WTe$_2$ crystal symmetries, for a current in a ($\hat{x}$) only the spin-polarization component along b ($\hat{y}$) is allowed: the ISGE can generate a spin density in $\hat{y}$, while the spin Hall current flowing in $\hat{z}$ should also be polarized along $\hat{y}$ [60]. Therefore, the $\hat{x}$ and $\hat{z}$ components are not expected in the bulk of Td-WTe$_2$, which indicates that both originate from interfacial or proximity-induced effects in graphene considering the reduced symmetry of the heterostructure [60].

The symmetry of an heterostructure or thin crystal can be equal or lower than its bulk constituents, permitting additional non-zero spin polarization components. Indeed, in the graphene-WTe$_2$ interface, the glide symmetry is absent, leaving possibly only the single mirror symmetry plane M_a. As discussed in figure 1, the generation of a spin density in c ($\hat{z}$), when $\mathbf{j}_c$ is along a ($\hat{x}$), would then be allowed.

The spin density along $\hat{x}$ was previously observed in graphene-MoTe$_2$ and graphene-WTe$_2$ and was ascribed to the presence of an additional bulk mirror symmetry breaking induced by strain in the TMDC [34, 36]. In our experiments, Raman spectroscopy demonstrates that WTe$_2$ is not under strain (see supplementary material), making this explanation implausible. Alternatively, the spin density in $\hat{x}$ could be generated by a current component along $\hat{y}$. Recent theoretical works reported anisotropic SHE in WTe$_2$ and MoTe$_2$ as a function of charge current direction and Fermi energy position [61, 62]. However, the elongated geometry of our WTe$_2$ flake (figure 2(d)) implies that the current component along $\hat{y}$ is very small and a very large CSI efficiency would be required to make this scenario viable. These observations confirm that the spin density along $\hat{x}$ is likely generated in the proximitized graphene.

Recent first-principles calculations addressing the twist-angle dependence of proximity-induced SOC in graphene by TMDCs MoS$_2$, MoSe$_2$, WS$_2$ and WSe$_2$ have shown that the Rashba SOC could exhibit a radial component, thus deviating from the typical tangential orientation [37]. As discussed in references [35, 37], the radial component is allowed for twist angles between the graphene and TMDC lattices different from 0° and 30°, where mirror symmetries are broken and the point group symmetry of graphene-TMDC is reduced to C_3. Similarly, an arbitrary twist angle between the graphene and WTe$_2$ crystal lattices can break the remaining symmetry upon reflection in M_a. At their interface, with radial Rashba SOC coupling, a spin polarization component parallel to $\mathbf{j}_c$ can then arise.

It remains to be understood why the radial component has never been observed in graphene-WS$_2$ and graphene-MoS$_2$ [28–30]. The high annealing temperatures used in those works, to clean the heterostructures and improve the interface quality, might have favored 0° or 30° twist angles, although this argument would not be valid if the initial (arbitrary) twist angle was larger than perhaps a fraction of a degree. Therefore, further studies are required to address this question.

Finally, the observed spin current along $\hat{y}$, which is polarized in $\hat{z}$, has not been reported in prior graphene-WTe$_2$ studies [36, 46]. It is however allowed even in high-symmetry structures, and has been reported in graphene-MoS$_2$ and graphene-WS$_2$ [28–30]. In these experiments, the generation of a spin density with polarization in $\hat{y}$ was also found. It was further confirmed that both the spin current polarized in $\hat{z}$ and the spin density in $\hat{y}$ can originate solely from the SHE and the ISGE in proximitized graphene, respectively [28, 30]. But, in general, the former could be due to the SHE, in graphene or in the TMDC, while the latter to the ISGE in graphene or the SHE in the TMDC [29].

The previous discussion strongly suggests that the unconventional CSI components in graphene-WTe$_2$ originate from interfacial or proximity effects. In contrast, the observed spin current with polarization in $\hat{z}$ and the spin densities in $\hat{y}$ are permitted both in the bulk of Td-WTe$_2$ and in proximitized graphene. Quantifying the spin absorption in WTe$_2$ could in principle help separate these remaining CSI contributions, however, the analysis is not straightforward or free of ambiguities. The estimation of the spin absorption requires detailed knowledge of heterostructure properties that cannot be readily obtained in nonlocal devices. The properties include the precise interface resistance between graphene and WTe$_2$ as well as the spin relaxation parameters in both the proximitized graphene and WTe$_2$. Any subtle change in these parameters, or in the implementation of the spin absorption model, can result in diverging conclusions. In addition, due to the 2D nature of graphene, the spin absorption is not uniform at the graphene-WTe$_2$ interface, even if the spin-current absorption occurs in z direction. This can be easily understood by considering the inverse SHE, commonly used in CSI experiments. Because of spin relaxation and the fact that there is no alternative path for spins to cross the CSI region, as in a 3D system, the majority of spins will be absorbed on the side of graphene-WTe$_2$ that is closest to the FM injector. This leads to a spin accumulation gradient (and a spin current) in the TMDC along the spin channel.

3. Conclusions

We have demonstrated experimentally that the CSI in graphene-WTe$_2$, with a current along the WTe$_2$ *a* axis, induces spin-polarized carriers with polarization components in all three spatial directions. By implementing systematic multi-terminal nonlocal spin precession experiments, we have shown that it is possible to disentangle the CSI from the spin Hall and ISGEs. A spin current flowing along the graphene channel leads to opposite spin polarization on the two sides of the CSI region, inducing a signal with opposite sign in remote FM detectors at each side. In contrast, a spin density in the CSI region produces a signal with equal sign in the same detectors.

We confirmed a spin accumulation with polarization along the applied current, which by symmetry is not allowed in the WTe$_2$ bulk. Our analysis indicates that this spin accumulation originates at the graphene-WTe$_2$ interface and involves the emergence of a radial component in the proximity-induced Rashba SOC, which arises from twisting [35, 37]. To validate this interpretation, additional experiments are needed. In particular, the radial component was predicted to be extremely sensitive to the twist angle, unintended doping and carrier density [37]. Therefore, it is necessary to systematically address the dependence of the spin accumulation parallel to the current as a function of crystalline orientation, sample annealing temperature and gate voltage. For the latter, thin, ideally monolayer, WTe$_2$ should be used to avoid both gate shielding (from semi-metallic bulk WTe$_2$) and added complexity from spin absorption. Nevertheless, to unambiguously demonstrate the radial Rashba component, it might be better to simply focus on semiconducting TMDCs.

We also show, for the first time, the presence of spin currents and spin densities with polarization perpendicular to the substrate plane in graphene-WTe$_2$. The observed spin polarization, as generated by the SHE spin current is always allowed, and can be induced in the bulk of WTe$_2$ or in proximitized graphene. However, symmetry considerations show that the spin density with perpendicular polarization must originate from the ISGE at the graphene-WTe$_2$ interface.

Overall, our work demonstrates that multi-terminal CSI measurements combined with symmetry analysis are powerful approaches to discriminate CSI signals. This is important for both applied and fundamental reasons. In particular, understanding the CSI originating from SHE and ISGE with all possible orientations is a promising route for magnetic memory applications, where the generation of unconventional spin-orbit torques is required [38].

Overall, our work demonstrates that multi-terminal CSI measurements combined with symmetry analysis are powerful approaches to discriminate CSI signals. This is important for both applied and fundamental reasons. In particular, understanding the CSI originating from SHE and ISGE with all possible orientations is a promising route for magnetic memory applications, where the generation of unconventional spin-orbit torques is required [38].

Note added in proof: Related results show unconventional spin-to-charge conversion in graphene-NbSe$_2$ devices that are consistent with reduced symmetry at the twisted graphene/NbSe$_2$ interface [63].

Data availability statement

The data that support the findings of this study are available upon reasonable request from the authors.

Acknowledgments

ORCID iDs

Josef Světl'ík ⬤ https://orcid.org/0000-0002-5949-5525
Marius V Costache ⬤ https://orcid.org/0000-0001-7432-6175
Vera Marinova ⬤ https://orcid.org/0000-0002-3499-0212
Dimitre Dimitrov ⬤ https://orcid.org/0000-0001-7638-9567
Juan F Sierra ⬤ https://orcid.org/0000-0002-5438-0534
Sergio O Valenzuela ⬤ https://orcid.org/0000-0002-4632-8891

References

[1] Elliott R J 1954 Spin-orbit coupling in band theory-character tables for some "double" space groups *Phys. Rev.* **96** 280
[2] Zahid Hasan M and Kane C L 2010 Colloquium: topological insulators *Rev. Mod. Phys.* **82** 3045

[3] Bogdanov A N and Rößler U K 2001 Chiral symmetry breaking in magnetic thin films and multilayers *Phys. Rev. Lett.* **87** 037203

[4] Kane C L and Mele E J 2005 Z_2 topological order and the quantum spin Hall effect *Phys. Rev. Lett.* **95** 146802

[5] Chang C-Z and Li M 2016 Quantum anomalous Hall effect in time-reversal-symmetry breaking topological insulators *J. Phys.: Condens. Matter.* **28** 123002

[6] Manchon A, Koo H C, Nitta J, Frolov S M and Duine R A 2015 New perspectives for Rashba spin-orbit coupling *Nat. Mater.* **14** 871–82

[7] Sinova J, Valenzuela S O, Wunderlich Jorg, Back C H and Jungwirth T 2015 Spin Hall effects *Rev. Mod. Phys.* **87** 1213

[8] Soumyanarayanan A, Reyren N, Fert A and Panagopoulos C 2016 Emergent phenomena induced by spin-orbit coupling at surfaces and interfaces *Nature* **539** 509–17

[9] Galceran R *et al* 2021 Control of spin-charge conversion in van der Waals heterostructures *APL Mater.* **9** 100901

[10] D'Yakonov M I and Perel V I 1971 Possibility of orienting electron spins with current *Sov. J. Exp. Theor. Phys. Lett.* **13** 467 (available at: http://jetpletters.ru/ps/1587/article_24366.shtml)

[11] Dyakonov M I and Perel V I 1971 Current-induced spin orientation of electrons in semiconductors *Phys. Lett.* A **35** 459–60

[12] Hirsch J E 1999 Spin Hall effect *Phys. Rev. Lett.* **83** 1834

[13] Ganichev S D, Ivchenko E L, Bel'Kov V V, Tarasenko S A, Sollinger M, Weiss D, Wegscheider W and Prettl W 2002 Spin-galvanic effect *Nature* **417** 153–6

[14] Onsager L 1931 Reciprocal relations in irreversible processes. I *Phys. Rev.* **37** 405

[15] Jacquod P, Whitney R S, Meair J and Büttiker M 2012 Onsager relations in coupled electric, thermoelectric and spin transport: the tenfold way *Phys. Rev.* B **86** 155118

[16] Berry M V 1984 Quantal phase factors accompanying adiabatic changes *Proc. R. Soc.* A **392** 45–57

[17] Xiao Di, Chang M-C and Niu Q 2010 Berry phase effects on electronic properties *Rev. Mod. Phys.* **82** 1959

[18] Edelstein V M 1990 Spin polarization of conduction electrons induced by electric current in two-dimensional asymmetric electron systems *Solid State Commun.* **73** 233–5

[19] Luo J-W, Bester G and Zunger A 2009 Full-zone spin splitting for electrons and holes in bulk GaAs and GaSb *Phys. Rev. Lett.* **102** 056405

[20] Zhang X, Liu Q, Luo J-W, Freeman A J and Zunger A 2014 Hidden spin polarization in inversion-symmetric bulk crystals *Nat. Phys.* **10** 387–93

[21] Kato Y K, Myers R C, Gossard A C and Awschalom D D 2004 Observation of the spin Hall effect in semiconductors *Science* **306** 1910–3

[22] Wunderlich J, Kaestner B, Sinova J and Jungwirth T 2005 Experimental observation of the spin-Hall effect in a two-dimensional spin-orbit coupled semiconductor system *Phys. Rev. Lett.* **94** 047204

[23] Valenzuela S O and Tinkham M 2006 Direct electronic measurement of the spin Hall effect *Nature* **442** 176–9

[24] Saitoh E, Ueda M, Miyajima H and Tatara G 2006 Conversion of spin current into charge current at room temperature: inverse spin-Hall effect *Appl. Phys. Lett.* **88** 182509

[25] Kimura T, Otani Y, Sato T, Takahashi S and Maekawa S 2007 Room-temperature reversible spin Hall effect *Phys. Rev. Lett.* **98** 156601

[26] Dieny B *et al* 2020 Opportunities and challenges for spintronics in the microelectronics industry *Nat. Electron.* **3** 446–59

[27] Sierra J F, Fabian J, Kawakami R K, Roche S and Valenzuela S O 2020 Van der Waals heterostructures for spintronics and opto-spintronics *Nat. Nanotechnol.* **3** 446–59

[28] Ghiasi T S, Kaverzin A A, Blah P J and van Wees B J 2019 Charge-to-spin conversion by the Rashba-Edelstein effect in two-dimensional van der Waals heterostructures up to room temperature *Nano Lett.* **19** 5959–66

[29] Safeer C K, Ingla-Aynés J, Herling F, Garcia J H, Vila M, Ontoso N, Calvo M R, Roche S, Hueso L E and Casanova F 2019 Room-temperature spin Hall effect in graphene/MoS_2 van der Waals heterostructures *Nano Lett.* **19** 1074–82

[30] Antonio Benitez L, Torres W S, Sierra J F, Timmermans M, Garcia J H, Roche S, Costache M V and Valenzuela S O 2020 Tunable room-temperature spin galvanic and spin Hall effects in van der Waals heterostructures *Nat. Mater.* **19** 170–5

[31] Garcia J H, Cummings A W and Roche S 2017 Spin hall effect and weak antilocalization in graphene/transition metal dichalcogenide heterostructures *Nano Lett.* **17** 5078–83

[32] Offidani M, Milletarì M, Raimondi R and Ferreira A 2017 Optimal charge-to-spin conversion in graphene on transition-metal dichalcogenides *Phys. Rev. Lett.* **119** 196801

[33] Cavill S A, Huang C, Offidani M, Lin Y-H, Cazalilla M A and Ferreira A 2020 Proposal for unambiguous electrical detection of spin-charge conversion in lateral spin valves *Phys. Rev. Lett.* **124** 236803

[34] Safeer C K *et al* 2019 Large multidirectional spin-to-charge conversion in low-symmetry semimetal $MoTe_2$ at room temperature *Nano Lett.* **19** 8758–66

[35] Li Y and Koshino M 2019 Twist-angle dependence of the proximity spin-orbit coupling in graphene on transition-metal dichalcogenides *Phys. Rev.* B **99** 075438

[36] Zhao B, Karpiak B, Khokhriakov D, Johansson A, Hoque A M, Xu X, Jiang Y, Mertig I and Dash S P 2020 Unconventional charge-spin conversion in Weyl-semimetal WTe_2 *Adv. Mater.* **32** 2000818

[37] Naimer T, Zollner K, Gmitra M and Fabian J 2021 Twist-angle dependent proximity induced spin-orbit coupling in graphene/transition metal dichalcogenide heterostructures *Phys. Rev.* B **104** 195156

[38] MacNeill D, Stiehl G M, Guimaraes M H D, Buhrman R A, Park J and Ralph D C 2017 Control of spin-orbit torques through crystal symmetry in WTe_2/ferromagnet bilayers *Nat. Phys.* **13** 300–5

[39] Safeer C K, Herling F, Choi W Y, Ontoso N, Ingla-Aynés J, Hueso L E and Casanova F 2022 Reliability of spin-to-charge conversion measurements in graphene-based lateral spin valves *2D Mater.* **9** 015024

[40] Savero Torres W, Sierra J F, Benítez L A, Bonell F, Costache M V and Valenzuela S O 2017 Spin precession and spin Hall effect in monolayer graphene/Pt nanostructures *2D Mater.* **4** 041008

[41] Seemann M, Ködderitzsch D, Wimmer S and Ebert H 2015 Symmetry-imposed shape of linear response tensors *Phys. Rev.* B **92** 155138

[42] Roy A, Guimarães M H D and Sławińska J 2022 Unconventional spin Hall effects in nonmagnetic solids *Phys. Rev. Mater.* **6** 045004

[43] Bychkov Y A and Rashba E I 1984 Oscillatory effects and the magnetic susceptibility of carriers in inversion layers *J. Phys. C: Solid State Phys.* **17** 6039

[44] Bihlmayer G, Rader O and Winkler R 2015 Focus on the Rashba effect *New J. Phys.* **17** 050202

[45] Yan W, Sagasta E, Ribeiro M, Niimi Y, Hueso L E and Casanova F 2017 Large room temperature spin-to-charge conversion signals in a few-layer graphene/Pt lateral heterostructure *Nat. Commun.* **8** 661

[46] Zhao B, Khokhriakov D, Zhang Y, Fu H, Karpiak B, Hoque A M, Xu X, Jiang Y, Yan B and Dash S P 2020 Observation of charge to spin conversion in Weyl semimetal WTe_2 at room temperature *Phys. Rev. Res.* **2** 013286

[47] Zhang S 2000 Spin Hall effect in the presence of spin diffusion *Phys. Rev. Lett.* **85** 393

[48] Stamm C, Murer C, Berritta M, Feng J, Gabureac M, Oppeneer P M and Gambardella P 2017 Magneto-optical detection of the spin Hall effect in pt and w thin films *Phys. Rev. Lett.* **119** 087203

[49] Torrey H C 1956 Bloch equations with diffusion terms *Phys. Rev.* **104** 563

[50] Johnson M and Silsbee R H 1988 Coupling of electronic charge and spin at a ferromagnetic–paramagnetic metal interface *Phys. Rev.* B **37** 5312

[51] Žutić I, Fabian J and Sarma S D 2004 Spintronics: fundamentals and applications *Rev. Mod. Phys.* **76** 323

[52] Soluyanov A A, Gresch D, Wang Z, Wu Q, Troyer M, Dai X and Bernevig B A 2015 Type-II Weyl semimetals *Nature* **527** 495–8

[53] Li P, Wen Y, Xin H, Zhang Q, Xia C, Yu Z-M, Yang S A, Zhu Z, Alshareef H N and Zhang X-X 2017 Evidence for topological type-II Weyl semimetal WTe$_2$ *Nat. Commun.* **8** 2150

[54] Fei Z, Palomaki T, Wu S, Zhao W, Cai X, Sun B, Nguyen P, Finney J, Xu X and Cobden D H 2017 Edge conduction in monolayer WTe$_2$ *Nat. Phys.* **13** 677–82

[55] Tang S *et al* 2017 Quantum spin Hall state in monolayer 1T'-WTe$_2$ *Nat. Phys.* **13** 683–7

[56] Wu S, Fatemi V, Gibson Q D, Watanabe K, Taniguchi T, Cava R J and Jarillo-Herrero P 2018 Observation of the quantum spin Hall effect up to 100 kelvin in a monolayer crystal *Science* **359** 76–79

[57] Buchkov K, Todorov R, Terziyska P, Gospodinov M, Strijkova V, Dimitrov D and Marinova V 2021 Anisotropic optical response of WTe$_2$ single crystals studied by ellipsometric analysis *Nanomaterials* **11** 2262

[58] Song Q *et al* 2016 The in-plane anisotropy of WTe$_2$ investigated by angle-dependent and polarized Raman spectroscopy *Sci. Rep.* **6** 29254

[59] Raes B , Scheerder J E, Costache M V, Bonell F, Sierra J F, Cuppens J, Van de Vondel J and Valenzuela S O 2016 Determination of the spin-lifetime anisotropy in graphene using oblique spin precession *Nat. Commun.* **7** 11444

[60] Xue F and Haney P M 2020 Staggered spin Hall conductivity *Phys. Rev.* B **102** 195146

[61] Zhou J, Qiao J, Bournel A and Zhao W 2019 Intrinsic spin Hall conductivity of the semimetals MoTe$_2$ and WTe$_2$ *Phys. Rev.* B **99** 060408

[62] Vila M , Hsu C-H, Garcia J H, Benítez L A, Waintal X, Valenzuela S O, Pereira V M and Roche S 2021 Low-symmetry topological materials for large charge-to-spin interconversion: the case of transition metal dichalcogenide monolayers *Phys. Rev. Res.* **3** 043230

[63] Ingla-Aynés J Inge G, Franz H, Nerea O, Safeer C K, Fernando de Juan, Luis E H, Marco G, Fèlix C 2022 Omnidirectional spin-to-charge conversion in graphene/NbSe2 van der Waals heterostructures (arxiv:2205.07668)